

Validation of the Effective Resolution of SMAP Enhanced Resolution Backscatter Products

David G. Long , Fellow, IEEE, and Julie Z. Miller 

Abstract—NASA’s Soil Moisture Active Passive (SMAP) mission originally included both passive and active L -band measurement capabilities. It was the first satellite instrument to provide global L -band radar observations of normalized radar cross section (σ^0) at multiple resolutions. The SMAP radar collected high-resolution (~ 1 – 3 km) synthetic aperture radar (SAR) measurements over most of the earth’s land mass. It simultaneously collected low-resolution 6×30 km “slice” and full-footprint 29×35 km measurements. The SMAP radar operated for 83 days, from day of the year 103 to 186 in 2015, before the transmitter failed. The SMAP radar was designed to make vegetation roughness measurements in support of the SMAP primary mission to measure soil moisture, but the radar data are useful for a variety of applications, particularly in the polar regions. Unfortunately, limitations in the data download volume precluded the downlink of high-resolution data over Antarctica, sea ice in the polar regions, and various islands. Nonetheless, low-resolution slice and footprint data were collected and downlinked over these areas. To better exploit these low-resolution data, this article employs image reconstruction techniques to create twice-daily enhanced resolution SMAP radar images from the slice and footprint measurements. To validate the resolution enhancement, the enhanced resolution data are compared to SAR results over Greenland and South America. The new dataset is provided to the science community to support cryosphere and climate studies.

Index Terms—CETB, L -band, radar, reconstruction, resolution enhancement, SETB, Soil Moisture Active Passive (SMAP).

I. INTRODUCTION

THE NASA Soil Moisture Active Passive (SMAP) mission, launched in 2015, was originally developed to measure soil moisture [1]. It included both passive (radiometer) and active (radar) channels operating at the L -band. The SMAP radar collected high-resolution (~ 1 – 3 km) synthetic aperture radar (SAR) normalized radar cross section (σ^0) measurements over most of the earth’s land mass. The radar collected global low-resolution 6×30 km “slice” and full-footprint 29×35 km σ^0 measurements. Unfortunately, the SMAP radar transmitter

failed after 83 days of operation, though the radiometer continues operation to the present (2022).

SMAP radar σ^0 measurements have application in soil moisture estimation [1], estimating near-surface wind speed over the ocean [2], sea ice mapping [1], and inferring freeze/thaw state [3]. Because the L -band radar signal penetrates deeply into ice and firn, the data have recently proven useful in mapping glacial aquifers [4], [5]. Unfortunately, data volume limitations for SMAP precluded the collection of high-resolution SAR σ^0 over Antarctica, and only low-resolution slice and footprint data were collected there.

In this article, we create a set of twice-daily SMAP σ^0 image products that are compatible with the NASA MEaSUREs Calibrated Passive Microwave Daily EASE-Grid 2.0 Brightness Temperature (CETB) Earth System Data Record (ESDR) [10] that provides cross-calibrated satellite radiometer TB images over a multidecadal period to support climate science studies, particularly in the polar regions. Our new SMAP σ^0 image products include global and polar map projections separately made from SAR, slice, and footprint measurements and are designed to make SMAP backscatter data readily available to support polar science.

In order to facilitate the use of the low-resolution measurements in such studies, we apply processing algorithms that enhance the spatial resolution of the slice and footprint measurements, particularly in Antarctica where the high-resolution SMAP L -band σ^0 measurements are not available. The resolution enhancement takes advantage of the swath overlap over the imaging period. In conducting this work, we found that the different characteristics of the SMAP SAR, slice, and footprint products can be exploited to generate additional radar products and describe the observed scattering characteristics over the great ice sheets (GI) of Antarctica and Greenland. We validate the effectiveness of the resolution enhancement by the comparison of SAR and low-resolution slice and footprint data in regions where both data are available. It is our hope that the new and unique products can support a wider variety of studies of the cryosphere.

The rest of this article is organized as follows. We first provide general background on SMAP, CETB, and scatterometer reconstruction and resolution enhancement. We then consider a simple model for the incidence and azimuth angle dependence of σ^0 over the GI and how the model parameters can be estimated from SMAP radar data. The observation of local time of day (LTOD) is next considered. A comparison of SAR and enhanced resolution slice and footprint images is presented to

Manuscript received 29 July 2022; revised 12 November 2022 and 25 February 2023; accepted 20 March 2023. Date of publication 23 March 2023; date of current version 7 April 2023. This work was supported in part by the NASA Science Team under Grant 80NSSC20K1806. (Corresponding author: David G. Long.)

David G. Long is with the Department of Electrical and Computer Engineering, Brigham Young University, Provo, UT 84602 USA (e-mail: long@ee.byu.edu).

Julie Z. Miller is with the Earth Science and Observation Center, Cooperative Institute for Research in Environmental Sciences, University of Colorado, Boulder, CO 80309 USA (e-mail: jzmiller.research@gmail.com).

Digital Object Identifier 10.1109/JSTARS.2023.3260726

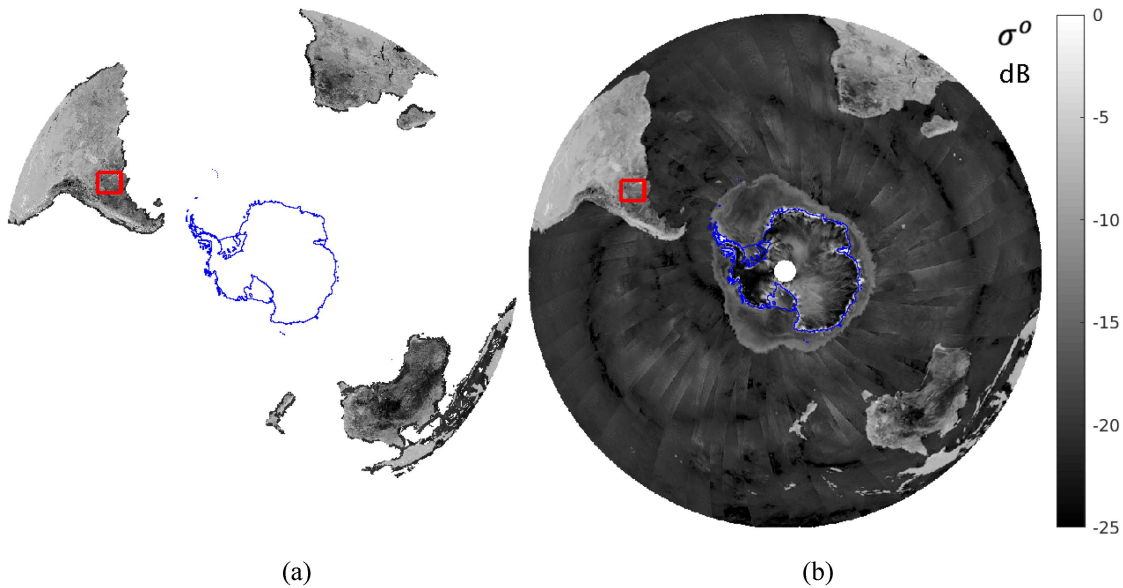


Fig. 1. Southern Hemisphere coverage for eight days of data (the orbit repeat cycle) for (a) SMAP SAR and (b) SMAP footprint showing σ^0 in dB. Image shown is evening LTOD, HH polarization, but coverage is the same for all polarizations. Note the lack of SAR coverage over Antarctica and smaller islands. The red box shows the location of the Argentine study area. At this scale, the corresponding SMAP slice σ^0 image appear identical to the SMAP footprint image and so is not shown.

validate the performance of the resolution enhancement. Finally, a summary is provided. Data products from this research are available from the National Snow and Ice Data Center (NSIDC) (<https://nsidc.org/data/NSIDC-0738/versions/1>) [9].

II. BACKGROUND

A. SMAP Radar

Data for this study come from the SMAP radar. The SMAP radar is uniquely qualified for this study because of the availability of SMAP high-resolution SAR images that can be used to quantify the reconstruction performance of the low-resolution data in selected areas, such as Greenland. Fig. 1 compares the typical Southern Hemisphere coverage for SMAP radar SAR and slice/footprint measurements over an eight-day period. While the SAR image clearly has finer effective resolution, it does not provide overage over Antarctica or over sea ice in either hemisphere. The lack of high-resolution coverage of Antarctica motivates our desire to enhance the resolution of the slice and footprint data.

The SMAP mission was launched in January 2015 and flies in a 98.1° inclination polar orbit at 685-km altitude. It includes both a radiometer and a radar that operate at L -band [1]. Though the radar only had a limited lifetime (83 days in 2015), the radiometer is currently operational [6]. The SMAP radar is unique in that three different kinds of radar measurements are collected simultaneously. The measurement kinds differed in the way that the data are processed in real time onboard and in ground processing, with advantages and disadvantages for each. The radar does this for each of four polarization combinations: horizontal–horizontal (HH), vertical–vertical (VV), and the cross polarizations HV and VH.

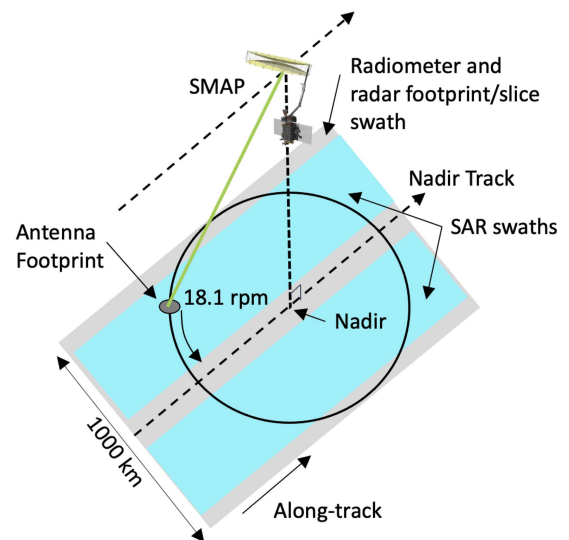


Fig. 2. SMAP swath layout. Radar footprint and slice and radiometer measurements are collected over a 1000-km swath. SAR measurements are not available over the central (nadir) portion of the swath.

The SMAP instrument is based on a 6-m conically scanning reflector antenna with a common L -band feed shared by the radar (~ 1.26 GHz) and radiometer (~ 1.41 GHz). The reflector rotates about the nadir axis, producing the conically scanning antenna beam with a one-way 3-dB effective field of view measuring 39×47 km at an Earth incidence angle of 40° at the beam center. The swath width is approximately 1000 km wide (see Fig. 2). The rotating antenna beam enables the sensor to look in both the fore and aft directions [6], [8]. Originally, SMAP products were produced using both radiometer and radar measurements [1].

B. CETB and SETB ESDRs

The CETB project team created a single, consistently processed, multisensor ESDR of Earth-gridded microwave brightness temperature (T_B) images spanning from 1978 to the present (2023) based on new fundamental climate data records for passive microwave observations from a wide array of sensors [7], [10], [11]. The CETB dataset includes both conventional and enhanced resolution T_B images on standard map projections and is designed to serve the land surface and polar snow/ice communities in studies of climate and climate change [12].

For each of the CETB sensors, T_B image products are created by mapping individual T_B measurements onto an Earth-based grid using *EASE-Grid 2.0* map projections [16], [17]. In the conventional-resolution gridded (GRD) CETB product, the center of each measurement location is mapped to an output projected grid cell or pixel. All the measurements within the specified time period whose centers fall within the bounds of a particular grid cell are averaged together. The unweighted average becomes the reported pixel T_B value for that grid cell. Since measurement footprints can extend outside of the pixel, the effective resolution of GRD images is coarser than the pixel size. To create finer resolution images, reconstruction techniques are employed [12]. Coarse and fine resolution images are produced on compatible map projections and grid spacings [10], [11]. A set of CETB-compatible SMAP radiometer (SETB) products are produced from the continuing SMAP radiometer mission [10]. For the SMAP radar, we follow a similar approach of generating coarse and fine-resolution twice-daily image products on the same map projection [9].

C. Pixel and Measurement Spatial Response Functions

The *effective resolution* of an image is defined by the *pixel spatial response function* (PSRF), where the effective resolution is given by the dimension(s) of the half power (3-dB) extent of the PSRF. In contrast, the *measurement response function* (MRF) describes the spatial characteristics of the *individual* measurements. For a radiometer measurement, the MRF is a “smeared” version of the one-way antenna pattern where the smearing is due to the movement of the antenna pattern on the surface over the measurement integration period [12]. For a radar, the MRF depends on the two-way antenna pattern, the modulation, and the signal processing. For both radiometers and radars, the PSRF depends on the MRF and the image formation algorithm.

In our case, multiple measurements (sometimes from different passes) are combined into single pixel values. For SAR, the image formation algorithm coherently (signal magnitude and phase) combines measurements to estimate σ^0 on a 1-km grid [8]. The resulting σ^0 values are then incoherently gridded onto a 3.125-km grid using a drop-in-the-bucket (DIB) technique. The resulting SAR pixels have an effective resolution slightly coarser than the pixel spacing of 3.125 km. For slice and footprint measurements, the image formation process is inherently incoherent, i.e., the σ^0 measurements (which are proportional to the signal power) are averaged. As a result, the

effective resolution of the slice and footprint measurements is much coarser than the SAR measurements, even when resolution enhancement is applied.

We call the spacing of pixels the “pixel posting” or the “posting resolution.” Note that the posting resolution is not necessarily the same as the effective resolution. In general, the effective resolution is coarser than the posting resolution (see [12]). In order to be compatible with the CETB and SETB dataset, two posting resolutions are considered: 25 and 3.125 km. In the CETB, the 25-km resolution is the base resolution with finer resolutions defined as powers of 2 division of the base resolution. The $3.125 = 25/8$ km resolution ensures that Nyquist requirements are met during the image processing.

To create SMAP radar CETB-compatible products, the SMAP SAR SL1CS0 [8], [18] measurements are regridded using DIB techniques onto a 3.125-km grid. For footprint and slice SL1BS0 [8], [19] measurements, the scatterometer image reconstruction (SIR) algorithm is applied on the same 3.125-km grid, but the results have coarser effective resolution. In addition, DIB gridding is used to create σ^0 images on 25-km grids for each measurement type. The SIR algorithm exploits the irregular patterns of measurement locations and signal oversampling (from overlaps in adjacent footprints and overlapping passes) [20], [22].

D. Reconstruction and Resolution Enhancement

A large number of papers have been written on the theory of radiometer and scatterometer resolution enhancement (see citations in [12] and [14]), including recent papers on SMAP radiometer reconstruction [10], [12], [14]. These algorithms exploit the measurement MRF pattern and measurement overlap to perform signal reconstruction to estimate σ^0 and T_B at finer resolution than the 3-dB width of the MRF. In effect, they “deconvolve” the PSRF to estimate the surface value at fine resolution pixels.

The iterative SIR algorithm employs regularization to trade off noise and resolution by limiting the number of iterations and thereby producing partial reconstruction and enhanced resolution [14], [20], [22]. SIR provides somewhat better results with less computation than competing algorithms [23]. The SIR products are posted on fine resolution grids with an effective resolution that is coarser than the posting resolution, i.e., they are oversampled. We note that the radiometer form of SIR was used for SETB products [12], [13], [20].

Following the SETB approach, we employ the SIR algorithm to estimate slice and footprint σ^0 values on a 3.125-km grid posting. The implementation of SIR for the SMAP radar is similar to that for QuikSCAT, as described in [22]. A brief summary is included in the Appendixes. SIR is an iterative algorithm that starts with an initial estimate. Termed “AVE” (for average), each pixel value in the AVE image is computed as the weighted average of the measurements that cover the pixel. The weighting is the MRF function of each measurement computed at the pixel center. The computation is done in dB. Given the initial estimate, the SIR algorithm computes the difference between

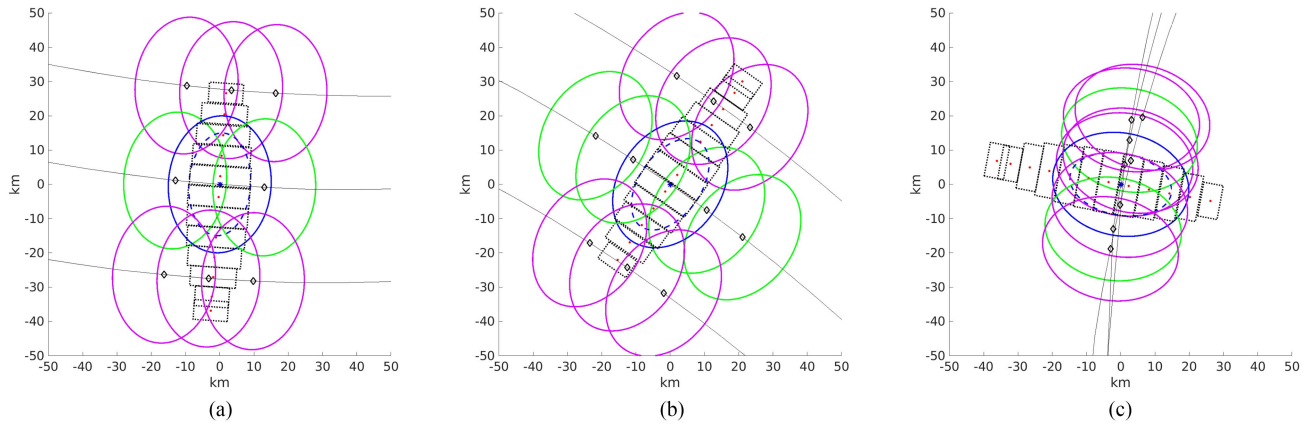


Fig. 3. Layout of the 3-dB outline of SMAP footprints and slices for different antenna rotation angles: (a) nadir swath, aft looking, (b) mid-side swath, aft looking, and (c) left-most swath. An asterisk at (0,0) is the center of the central measurement. Diamonds mark the locations of the footprint centers for consecutive pulses for three consecutive antenna rotations, with lines indicating the path of the beam center. The large ovals correspond to the radiometer (one-way) footprints, with the central measurement in blue, adjacent pulses in green, and pulses from the previous and next rotation in magenta. The small blue-dashed oval illustrates the radar (two-way) footprint for the central measurement. The dashed boxes illustrate the approximate slice responses, which are centered at the red dots. Note that the slices extend significantly outside the two-way radar footprint. The bottom two and top slices have significantly higher noise levels than the others that are not included in image formation. SAR measurements are reported on a 1 km \times 1 km map projection grid (not shown).

each measurement and its forward projection. The errors are then used to update the estimated σ^0 value for each pixel in the image. As part of this step, the error is nonlinearly damped to minimize the adverse effects of noise. The algorithm is regularized by stopping prior to convergence. Selecting the number of iterations at which the iteration is terminated affects the noise level and signal reconstruction error. More iterations minimize the signal error, but at the expense of additional noise enhancement since the reconstruction acts like a high-pass filter.

E. LTOD Data Division

As with prior radiometers in the CETB and for the SETB, in processing the SMAP data, we separately combine satellite orbital passes that occur between 00:00 and 12:00 and between 12:00 and 24:00 LTOD to generate twice-daily images that correspond to morning and evening (see Fig. 5). This minimizes fluctuations in the observed σ^0 at high latitudes due to daily temperature cycling. Fig. 4 illustrates the one-day coverage for each of the LTOD images. For SMAP, these two different time periods correspond to ascending/descending divisions. Histograms of the LTOD of SMAP observations fall within narrow latitude bands (70°–71°N and 71°–70°S), one for each hemisphere. Note how the LTOD falls within one of two tight groups with natural divisions in the measurement LTOD at 00:00 and 12:00 h. Thus, the measurements provide twice-daily sampling. Note that when data from multiple days are combined, the LTOD division is maintained so that a multiday morning image combines only morning observations.

III. IMAGE FORMATION METHODS

To create SMAP backscatter images, multiple methods are employed based on the SMAP measurement type. With a nominal PRF of approximately 2.8 kHz and pulse length of 15 μ s, the

SMAP radar produced σ^0 measurements at several resolutions: SAR, footprint, and slices. The highest resolution, which is available over only selected areas, is processed using an unfocused SAR algorithm to yield an effective resolution of about 1–3 km on a 1-km posting grid. This is the SL1CS0 source dataset [8], [18] for the SAR-based product images. Global radar data are also collected in a scatterometer mode at both footprint and slice resolutions' source in the SL1BS0 input dataset. For both the datasets, the raw measurements are processed into σ^0 values during ground processing [8]. Fig. 3 illustrates the spatial layout of multiple footprints and slices at different antenna rotation (scan) angles. Note the variable geometry due to the antenna rotation about the nadir point.

To create SMAP radar CETB-compatible products, the SMAP SAR SL1CS0 measurements are regridded using DIB onto 3.125- and 25-km grids. Footprint and slice SL1BS0 measurements are DIB regridded onto 25-km grids, with AVE and SIR used to produce 3.125-km images. Three temporal imaging periods were used: one-day, three-day, and eight-day with each divided into morning and evening LTOD. The one-day and three-day periods provide fine temporal resolution, while the eight-day period, which is the repeat orbit cycle, supports the scattering modeling described below.

With three input measurement types (SAR, slice, and footprint), multiple imaging periods (one, three, and eight days), and two output resolutions (3.125 and 25 km), different image formation algorithms are used as appropriate for each case. Table IV in Appendix A summarizes the image product types. Simple GRD images are created using DIB techniques at 25 and 3.125 km. In DIB, the measurements whose center falls within a given pixel area are averaged. AVE images use weighted averages where the weighting is the measurement MRF, which may vary from measurement to measurement. It is used for short-time slice images and for estimating scattering model

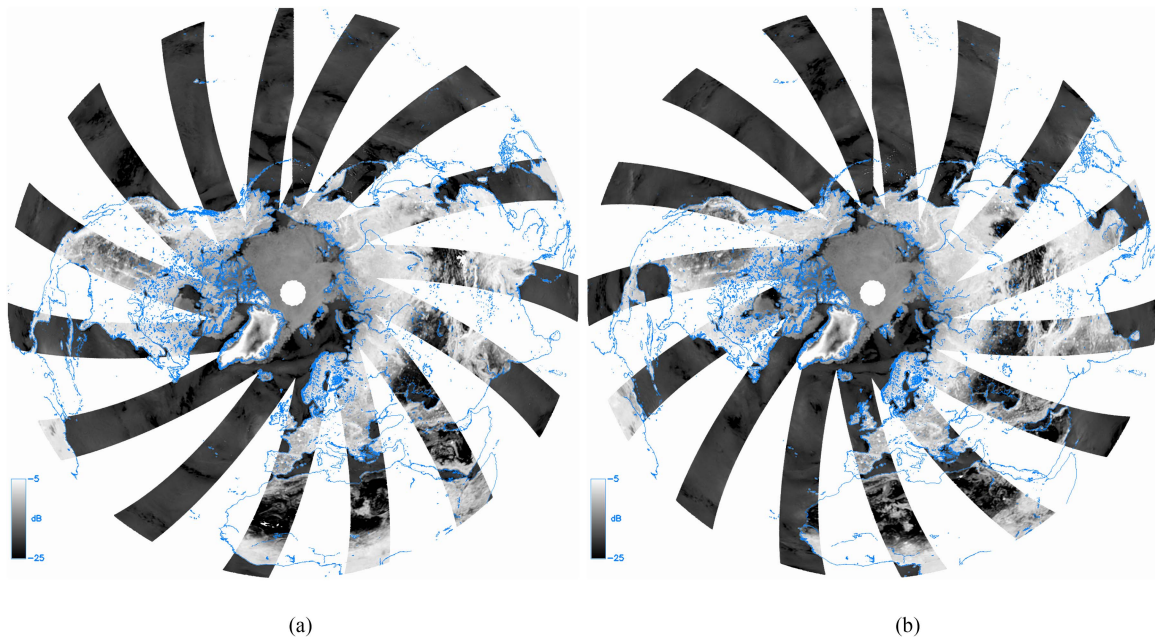


Fig. 4. Northern Hemisphere radar footprint coverage for a single day for (a) morning (00:00 to 12:00) and (b) evening (12:00 to 24:00) LTOD time periods. σ^0 in dB is shown for day 151, 2015 HH pol. Other polarizations have the same coverage.

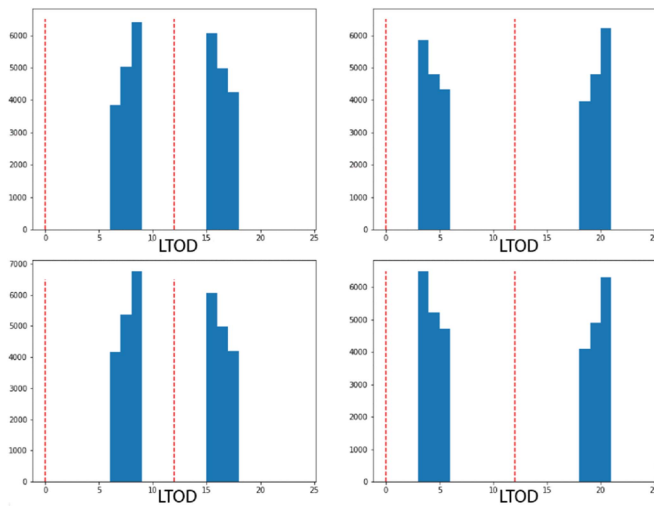


Fig. 5. Histograms of the measurement LTOD for SMAP measurements falling within a 1° latitude band at (top row) 70° – 71° N and (bottom row) 70° – 71° S for one day. Other days are similar. Note that all the measurements fall into only one of two narrow LTOD time periods centered at approximately 08:00 and 16:00 h in the Northern Hemisphere (left column) and 04:00 and 20:00 h in the Southern Hemisphere (right column). For any latitude, a given point is observed at one of two times within ± 90 min.

parameters (see below). The SIR algorithm is employed for slice and footprint images on the 3.125-km pixel grid.

Fig. 6 compares images of σ^0 over a selected area for each measurement type. In this and other images shown, HH pol evening LTOD images are used. The SAR image clearly has the best spatial resolution and dynamic range, but is not available over Antarctica. When not available, one of the other images must be chosen. Understanding the differences between the

TABLE I
SUMMARY DIFFERENCE STATISTICS COMPARED TO THE EIGHT-DAY 3.125-KM
REFERENCE SAR IMAGE

days	Measurement type	Algorithm	mean	STD
3	Footprint	GRD	0.158	0.435
3	Slice	GRD	0.111	0.316
3	Footprint	SIR	0.706	3.428
3	Slice	AVE	0.588	3.278
8	Slice	SIR	0.368	1.965

SAR, slice, and footprint images in Greenland provides insight into the performance of the slice and footprint images in Antarctica. As shown below, the slice data also provide the full set of scattering model parameter estimates described below that are unavailable with the other measurement types.

For studying the performance of the AVE and SIR reconstructions, the 3.125-km SAR image is used as a reference since it has the highest effective spatial resolution. Fig. 8 compares the various images. Difference statistics are computed for pixels over land and are shown in Table I. Unsurprisingly, the GRD images, which have the greatest averaging, but lowest resolution, have the smallest differences. The SIR images, which exhibit finer detail than GRD, have somewhat larger differences, with slice SIR having the smallest errors of the reconstruction images.

IV. MEASUREMENT MODELING

To dive deeper into the SMAP radar data and the performance of the imaging algorithms, we define some small study regions over the Greenland ICE SHEET (see Fig. 9). The regions are individually small enough to have nearly constant scattering characteristics, but span the range of ice facies over the ICE SHEET with a variety of mean σ^0 values. The location of a section

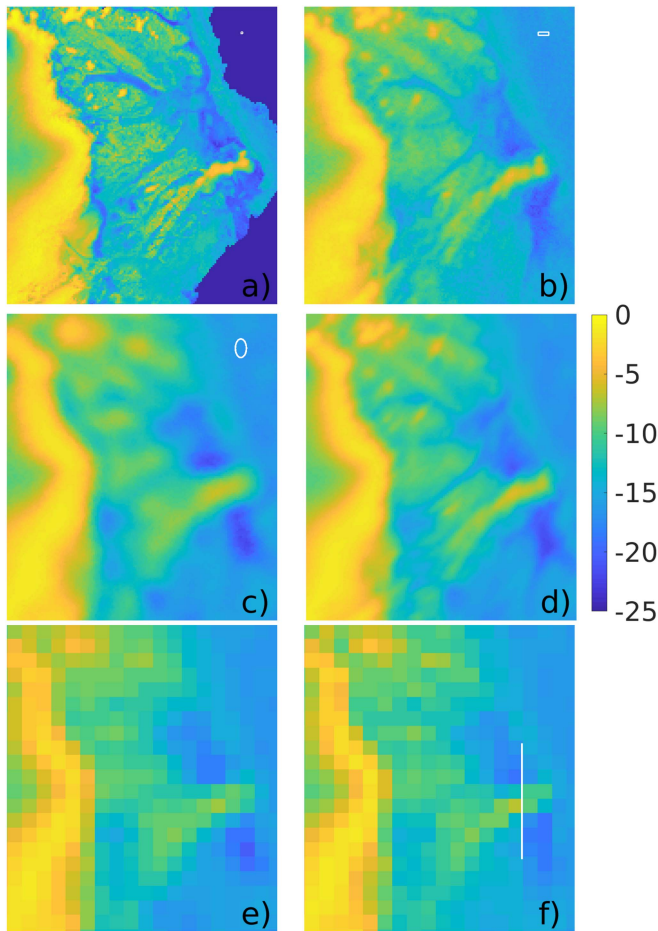


Fig. 6. Product comparison examples showing σ^0 in dB for a zoom-in area in North East Greenland. See Fig. 7 for location. (a) Eight-day 3.125-km SAR GRD. (b) Eight-day 3.125-km slice SIR. (c) Three-day 3.125-km footprint SIR. (d) Three-day 3.125-km slice AVE. (e) Three-day 25-km footprint GRD. (f) Three-day 25-km slice GRD. The small white box in (a) shows the size of a 3.125-km pixel. The small white rectangle in (b) represents the size of a typical slice. The small white oval in (c) is the size of the two-way radar footprint. The white line in (f) shows the location of a section line used later for evaluating image resolution.

line across the ice sheet is also shown, with a plot of σ^0 versus displacement from the center of the line shown in Fig. 10 for each of the σ^0 products. Each of the imaging algorithms has its advantages and disadvantages. In Fig. 10, the algorithms track each other closely, except beyond 500 km. At this point, the SAR coverage does not extend far enough out to include sea ice of the east coast, whereas the slice and footprint images do cover this area. One of the advantages of the slice and footprint images over the SAR image is their coverage. On the other hand, over the ice sheet, the very fine resolution of the SAR image shows some dips and peaks in σ^0 that are not fully represented by the coarser resolution of the slice and footprint images, particularly in the highly variable near-coastal area between 300 and 500 km. While the resolution differences probably account for most of the differences, there may be contributions due to the higher noise level of the SAR images compared to the slice and footprint images.

TABLE II
VALUES OF M124 MODEL COEFFICIENTS FOR EACH GREENLAND STUDY REGION FOR EACH MEASUREMENT TYPE

Type/ Region	M124 Model Coefficient Values							
	A_0 dB	A_1 dB	P_1 deg	A_2 dB	P_1 deg	A_4 dB	P_4 deg	B db/deg
SAR								
1	-1.71	0.564	85.4	0.072	129.2	0.043	90.3	+0.043
2	-3.58	0.277	105.0	0.064	-151.7	0.045	-37.2	-0.027
3	-7.69	0.278	147.0	0.087	-13.7	0.093	-22.8	-0.036
4	-9.97	0.165	130.5	0.046	-23.2	0.103	45.4	+0.074
5	-12.35	0.081	54.5	0.160	-46.5	0.059	64.4	+0.053
6	-18.64	0.455	59.4	0.184	75.6	0.223	-156.7	-0.088
7	-18.24	0.308	-143.1	0.784	-80.0	0.457	35.9	+0.268
8	-12.95	0.746	-173.8	0.353	95.9	0.059	-169.8	-0.010
9	-9.16	0.526	117.8	0.278	112.9	0.138	-83.1	-0.137
Slice								
1	-1.69	0.395	92.0	0.102	-104.2	0.264	92.1	+0.264
2	-4.27	0.146	105.2	0.097	-61.3	1.110	-88.8	-1.110
3	-10.09	0.311	133.6	0.136	-78.7	0.492	-78.4	-0.482
4	-13.28	0.236	136.3	0.177	-83.9	0.719	-99.5	-0.709
5	-16.28	0.183	57.5	0.162	-74.6	0.683	-68.3	-0.635
6	-20.67	0.389	18.4	0.041	-80.7	0.549	-79.5	-0.540
7	-20.05	0.324	161.8	0.177	3.9	0.445	155.8	+0.183
8	-15.65	0.929	-168.9	0.347	7.1	0.904	-171.5	-0.134
9	-10.81	0.665	58.0	0.319	167.3	2.234	129.2	+1.730
Foot								
1	-1.59	0.529	87.8	0.054	153.1	0.210	136.0	0.000
2	-3.18	0.296	94.8	0.044	167.9	0.450	-26.7	0.000
3	-7.35	0.298	127.3	0.094	-82.1	0.185	-50.5	0.000
4	-9.59	0.149	114.2	0.101	-151.0	0.232	-54.0	0.000
5	-12.03	0.121	20.7	0.070	+13.8	0.244	-22.4	0.000
6	-17.22	0.234	33.7	0.044	-79.7	0.243	-24.9	0.000
7	-17.73	0.203	175.9	0.120	-61.2	0.305	-123.9	0.000
8	-12.99	0.366	-160.5	0.389	-30.4	0.233	-159.4	0.000
9	-8.09	0.520	127.7	0.308	-166.7	0.817	-171.9	0.000

A. Incidence Angle Effects

Over natural surfaces, σ^0 depends on the measurement incidence angle. Owing to the careful control of the SMAP spacecraft attitude, the incidence angle of the center of the antenna footprint varies by less than 1° over the orbit. However, within the footprint, the incidence angle varies by $\pm 2^\circ$. Within the footprint, there is also a small variation ($< 0.5^\circ$) in azimuth angle, but this is considered negligible. The incidence angle variation within the footprint affects both the SAR and the slice measurements since they resolve the antenna footprint into many individual smaller areas that have different mean incidence and azimuth angles that are reported in the respective data products. In contrast, footprint measurements integrate the echo return over the full footprint and report a single σ^0 , mean incidence angle, and mean azimuth angle value. In effect, footprint measurements average out the incidence angle dependence. To illustrate this, Fig. 11 shows the variation in incidence angle for measurements collected over each of the Greenland study regions for SAR, slice, and footprint measurements, respectively, during an eight-day interval. Note the higher variability in σ^0 in the SAR observations compared to the slice and footprint cases. This is attributed mainly to the higher noise level of the SAR measurements compared to the lower resolution (and, thus, more averaged) slice and footprint measurements.

Noting the sloping dependence of σ^0 with incidence angle in the SAR and slice cases, separate linear fits of σ^0 versus incidence angle are determined using σ^0 expressed in dB and as a nonlog (linear units) value. Note that over the study regions, both positive and negative slopes are observed (see the B value in the right column of Table II). We further note that for footprint measurements, the incidence angle variation is too small to make a reliable slope estimate, and therefore, the slope, denoted by B , is treated as zero.

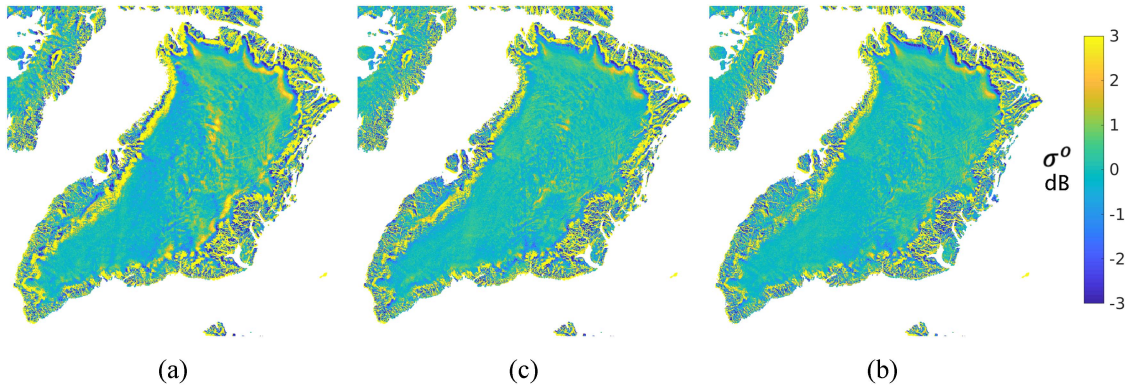


Fig. 8. σ^0 difference images over land between algorithm image and 3.125-km SAR reference image. (a) Three-day footprint SIR. (b) Three-day slice AVE. (c) Eight-day slice SIR. Images have been land masked. Difference statistics are summarized in Table I.

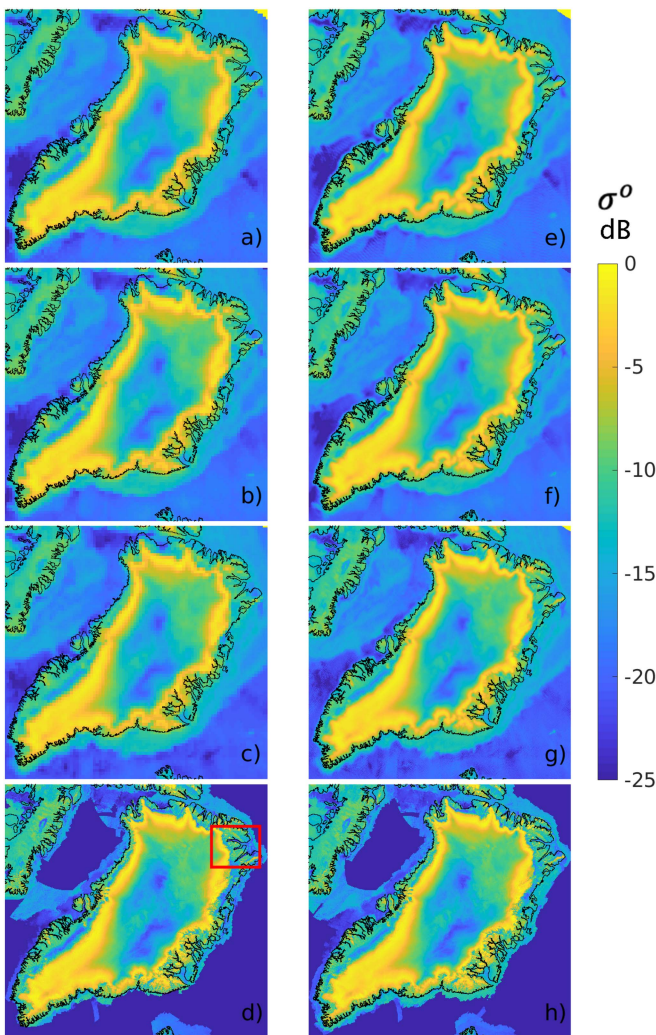


Fig. 7. Evening LTOD, HH pol σ^0 in dB images at different resolutions from different measurement types. (a) Three-day 25-km footprint GRD. (b) Three-day 25-km slice GRD. (c) Three-day 25-km SAR GRD. (d) Three-day 3.125-km SAR GRD. (e) Three-day 3.125-km footprint SIR. (f) Three-day 3.125-km slice AVE. (g) Eight-day 3.125-km slice SIR. (h) Eight-day 3.125-km SAR GRD. At the printed resolution, it is difficult to see the difference in the images. The red box shows the location of the zoom-in area comparisons in Figs. 6 and 9.

The incidence angle normalization $\gamma^o = \sigma^o / \cos \theta$, where θ is the incidence angle, is sometimes used. However, the slope of this correction is strictly downward, and upward slopes are observed in many areas. Thus, this normalization is not used. Instead, a linear slope is adequate for quantifying and correcting for incidence angle variations over the narrow range of incidence angles of the SMAP measurements.

B. Azimuth Angle Effects

Periodic natural surfaces exhibit variations in σ^0 with azimuth angle. Because the SMAP radar employs a rotating pencil-beam antenna, over the course of the orbit's eight-day repeat cycle, each point on the surface is observed at multiple azimuth angles. For example, as the spacecraft passes over a particular location within the swath, the location is first observed forward, then a short, while later the same location is observed backward. Over the eight-day orbit repeat cycle, the ground track shifts so that the same location is observed from a different set of azimuth angles for each pass. The precise distribution of azimuth angles depends on the orbit latitude, with the narrowest range near the equator and the largest range at high latitudes. This multiple-azimuth-angle capability provides a unique opportunity to study the azimuth angle variation of σ^0 at the L -band. Note that there is a tradeoff between the time period and the azimuth sampling. Short time periods provide better temporal resolution for tracking sea ice motion and rapid freeze/thaw events. However, short time periods provide inadequate coverage and/or azimuth sampling to reliably estimate the azimuth angle variation, particularly when the data are divided by LTOD. Because an eight-day period provides the maximum azimuth angle sampling, this period was used in the study when estimating and compensating for azimuth and incidence angle effects. To support studies requiring better temporal resolution that can ignore azimuth angle variation, we also created selected image products with one-day and three-day periods. In creating a time series, a "moving average" approach was used with overlapping imaging periods that start every mission day and extend through the desired one-, three-, or eight-day period (or to the end of the mission, whichever comes first).

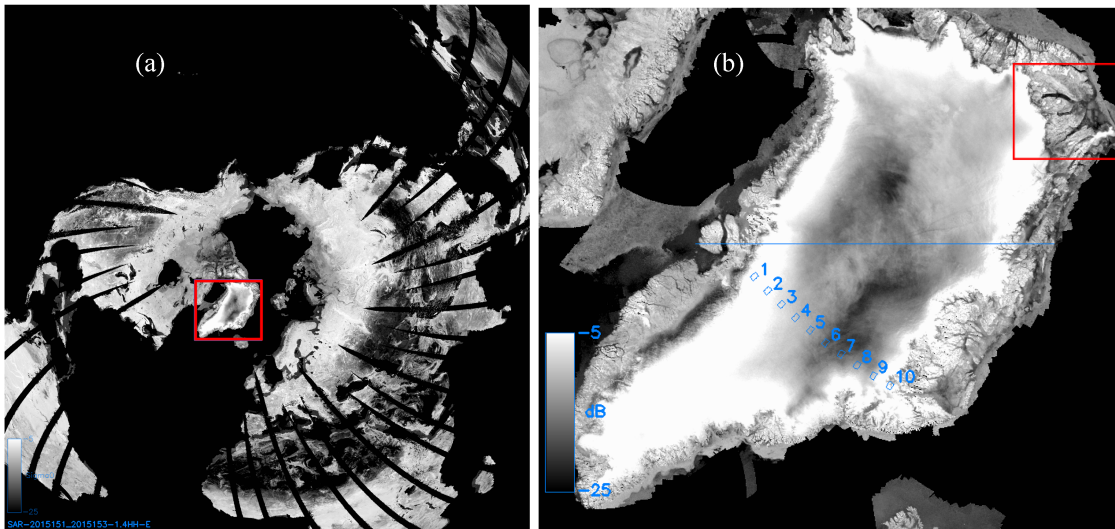


Fig. 9. (a) Three-day evening, HH pol SAR σ^0 (in dB) image of the Northern Hemisphere with Greenland study area indicated with red box. (b) Zoom in of red box in (a) showing the location of ten subareas as small boxes and a horizontal line segment showing the location of line section plotted in Fig. 10.

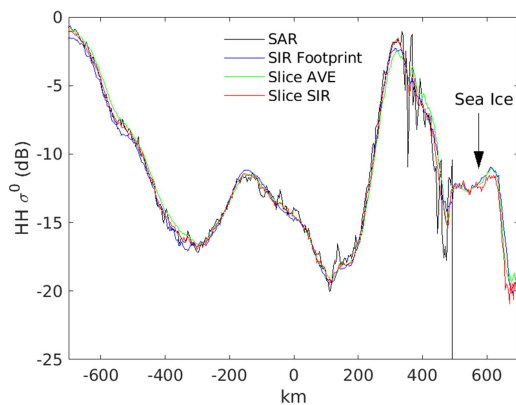


Fig. 10. Plot of evening LTOD three-day, HH σ^0 for various image products versus distance along an arbitrary line section crossing Greenland. See Fig. 9 for map of line location. Note that the SAR data do not extend far from the coast and so do not cover the full extent of sea ice off the east coast.

Note that a particular σ^0 observation is an average of σ^0 in spatial coordinates as well as in azimuth and incidence angles. The azimuth angle span for a given measurement is small and can be neglected. On the other hand, the variation in σ^0 as a function of azimuth angle for different measurements is important and can provide useful geophysical information, e.g., wind over the ocean [2], snow dunes and sastrugi [24], [27], and sand dunes [30]. Since each satellite pass observes a given point on the surface from a limited azimuth angle range, the variation of σ^0 with azimuth can lead to biases in the mean σ^0 value and to imaging artifacts when multiple passes with different azimuth angle observations are combined. To deal with azimuth variation of σ^0 over the GI, previous investigators (see, e.g., [24], [27], [28], and [29]) used a Fourier series model for the azimuth variation observed in σ^0 . Following their work, we use a similar approach for modeling the azimuth variation in σ^0 .

This technique, while applied globally, is most useful over the GI in the polar regions. Over the ocean and over other land areas, the amplitude of azimuth angle variation is very small, and the directional angle estimates reveal swath-related artifacts.

Fig. 11 shows the variation in σ^0 versus azimuth angle for the Greenland study regions for SAR, slice, and footprint measurements, respectively. σ^0 have been corrected for incidence angle using the fits determined earlier. Note the higher variability in σ^0 in the SAR observations compared to the slice and footprint cases. This is attributed mainly to the higher noise level of the SAR measurements compared to the lower resolution (and, thus, more averaged) slice and footprint measurements. Also note the declining number of measurements with coarse measurement resolution. All the cases exhibit a smoothed variation with azimuth angle of less than 1 dB for SAR and footprint measurements and up to 3 dB for slice measurements with the variation of σ^0 generally well described by a simple harmonic model.

C. Incidence/Azimuth Models

To account for the azimuth modulation behavior, the observed σ^0 is modeled as

$$\sigma^0 = A_0 + B(\theta - 40^\circ) + A_1 \cos(\phi + P_1) + A_2 \cos(2\phi + P_2) + A_4 \cos(4\phi + P_4) \quad (1)$$

where A_0 is the mean σ^0 ; B is the slope of σ^0 versus incidence angle θ normalized to 40° ; ϕ is the azimuth angle of the radar illumination relative to north; and A_1 , A_2 , and A_4 are the amplitudes and P_1 , P_2 , and P_4 are the phases of the first-, second-, and fourth-order azimuth modulation terms, respectively. Table II lists the values of the scattering model coefficients for each of the small Greenland study regions. We note that significant azimuth variation is common over the GI, but is only rarely observed elsewhere over large regions.

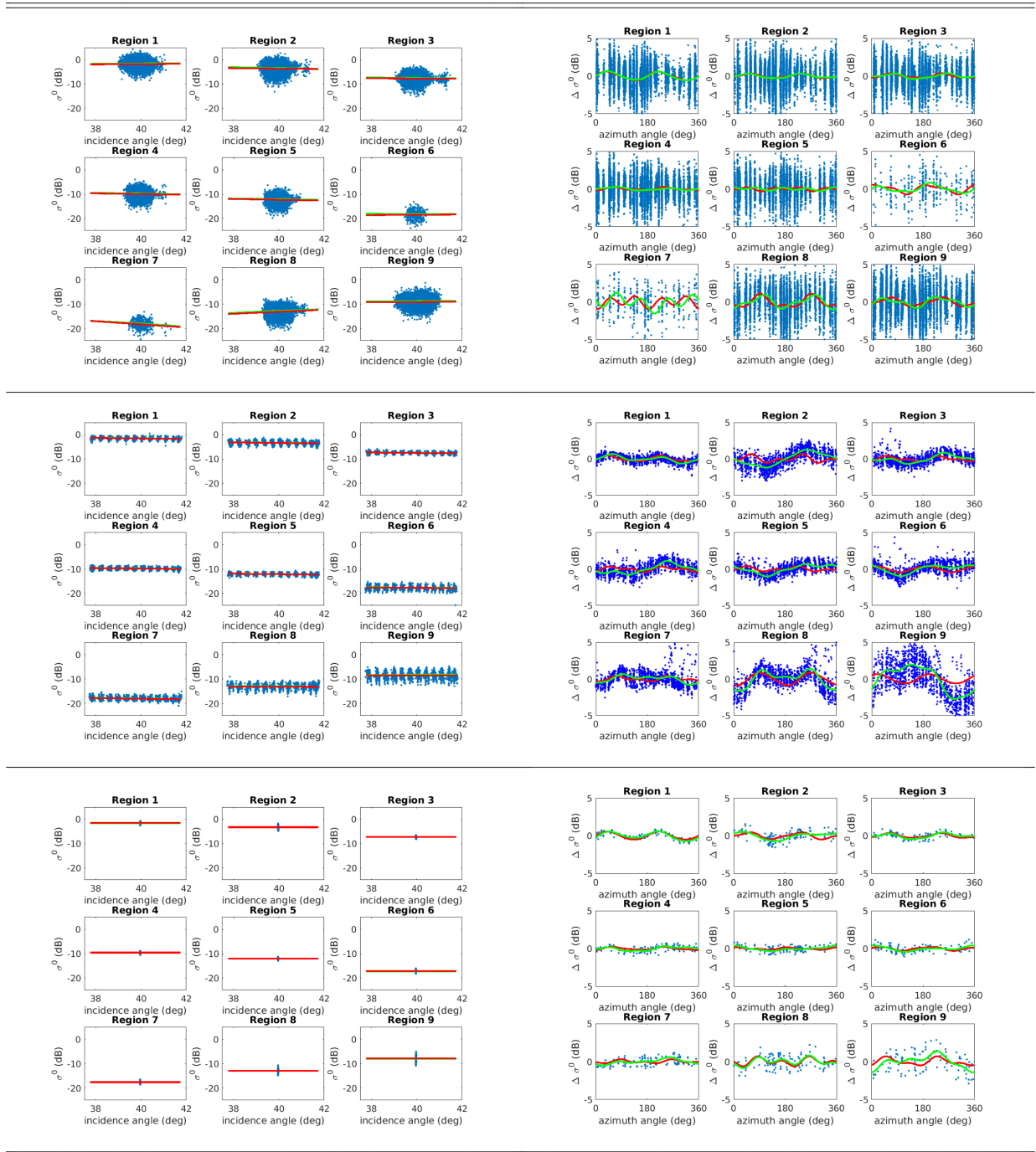


Fig. 11. Evening LTOD, HH σ^0 for each study region versus (left column) incidence angle showing linear (g) and dB (r) model fits and (right column) azimuth angle showing MI124 (g) and MI24 (r) model fits. (Top row) SAR, (middle row) slice, and (bottom row) footprint measurements.

At each pixel, the model parameters A_0 , B , A_1 , P_1 , A_2 , P_2 , A_4 , and P_4 are estimated from slice measurements. These values are reported in the slice products. Examples of these values for Antarctica and Greenland are shown in Figs. 12 and 13, respectively. Note the greater mean azimuth variation in Antarctica relative to Greenland. Table II lists the values of the scattering model coefficients for each of the Greenland study regions. Table III summarizes the statistics of the model fit for different model orders.

The various models are denoted by M for mean-only (i.e., only A_0 used, with other values treated as zero); MI for mean and incidence angle (i.e., only A_0 and B are used); MI24 that includes mean, incidence angle dependence, and second- and fourth-order azimuth terms (i.e., A_0 , B , A_2 , P_2 , A_4 , and P_4), and MI124 that includes all the parameters.

In Fig. 11, we observe that most of the azimuth variation is covered using only second- and fourth-order terms (the red curve), though some regions (notably 8 and 9) benefit from in-

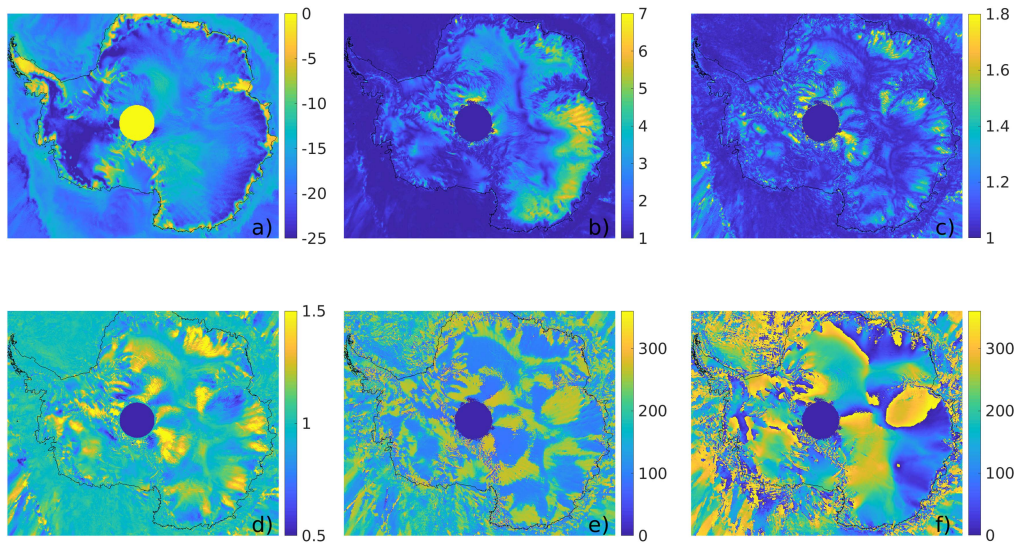


Fig. 12. Plot of evening LTOD, HH eight-day σ^0 azimuth and incidence angle variation images for Antarctica. (a) Mean σ^0 in dB. (b) A_2 in dB. (c) A_4 in dB. (d) B in dB/degree. (e) P_1 in degree. (f) P_2 in degree.

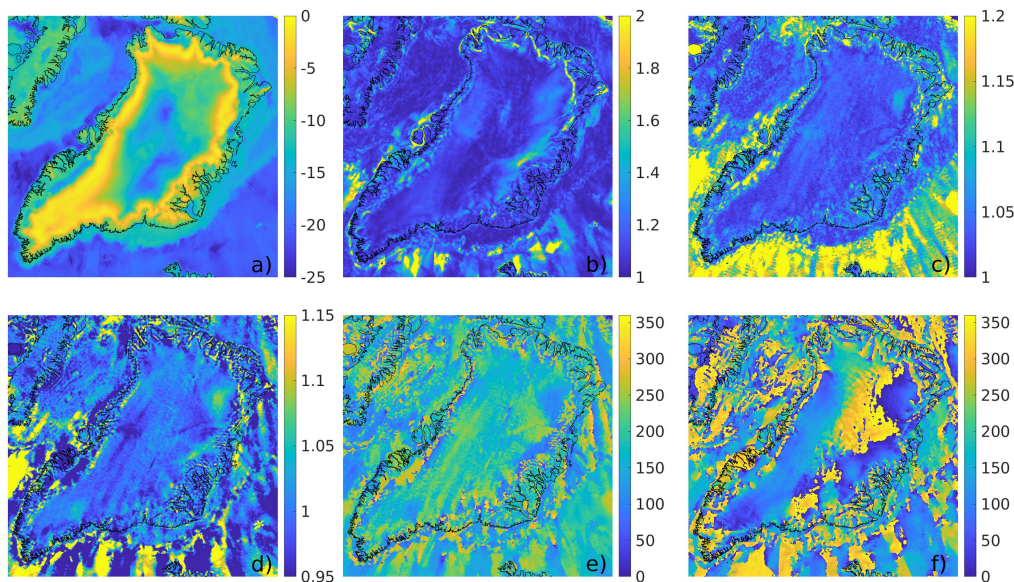


Fig. 13. Plot of evening LTOD, HH eight-day σ^0 azimuth and incidence angle variation images for Greenland. (a) Mean σ^0 in dB. (b) A_2 in dB. (c) A_4 in dB. (d) B in dB/degree. (e) P_1 in degree. (f) P_2 in degree.

cluding a first-order sinusoidal term (the green curve). Given the relatively small variation of the model parameters seen in these figures, the M model is used in SAR and footprint cases, i.e., the azimuth variation is ignored in image formation for processing these measurement types. Azimuth modeling is only included in processing slice measurements. Because the magnitude of A_1 is nominally small for most areas and including it the fit increases the estimate noise, we adopt the MI24 model for slice SIR processing. For each measurement, the pixels for which the measurement's MRF is nonnegligible are determined. Then, for each pixel, the MI24 model parameters are determined using least-squares estimation. The resulting model parameter images are median filtered using a 3×3 median filter to eliminate spike

artifacts that arise due to occasional inadequate observations that span the full range of possible azimuth and incidence angles. The resulting MI24 model parameter images are shown in Figs. 12 and 13. The MI24 model parameter images are included as ancillary images in the slice product files.

D. Model-Based Correction

The variation of σ^0 due to the azimuth and incidence angle variation is up to several dB. This can produce image artifacts when multiple measurements, which have different azimuth and incidence angles, are averaged into a pixel value. These artifacts are most apparent in short-period images. Such artifacts can be

TABLE III
RMS DIFFERENCE BETWEEN THE σ^0 MEASUREMENTS AND MODEL FITS FOR EACH STUDY REGION AND MEASUREMENT TYPE

Type/ Region	Count	Model			
		M	MI	MI24	MI124
SAR	63599	1.53	1.52	1.51	1.51
1	10905	1.35	1.35	1.30	1.30
2	12030	1.50	1.51	1.49	1.49
3	10656	1.41	1.40	1.40	1.39
4	8956	1.43	1.44	1.43	1.43
5	5823	1.51	1.51	1.52	1.50
6	378	1.74	1.73	1.71	1.71
7	453	1.70	1.71	1.79	1.74
8	5590	1.82	1.78	1.78	1.77
9	8808	1.79	1.77	1.75	1.76
Slice	10786	1.17	1.15	1.14	1.46
1	1261	0.46	0.51	0.42	0.60
2	1221	1.11	1.13	1.10	1.63
3	1195	0.70	0.72	0.70	0.79
4	1108	0.79	0.81	0.83	1.04
5	1145	0.75	0.79	0.75	0.92
6	1178	0.84	0.80	0.79	1.01
7	1299	1.05	1.03	1.05	1.05
8	1153	1.40	1.28	1.27	1.26
9	1226	2.29	2.26	2.25	3.11
Foot	1023	0.65	0.68	0.69	0.75
1	105	0.46	0.56	0.57	0.61
2	127	0.66	0.75	0.74	0.80
3	121	0.37	0.44	0.43	0.39
4	102	0.39	0.41	0.43	0.40
5	130	0.37	0.37	0.38	0.43
6	100	0.45	0.49	0.48	0.52
7	122	0.52	0.53	0.53	0.56
8	110	0.85	0.87	0.89	0.91
9	106	1.28	1.27	1.32	1.53

minimized by using the model parameters to adjust or correct for the dependence on measurement geometry. Unfortunately, the limited understanding of the effects of the SAR processing on the azimuth angle dependence prevent us from reliably applying the incidence/azimuth models to the SAR measurements. Furthermore, footprint measurements are at fixed incidence angles. We thus use the M model for the SAR and footprint cases, so that reported σ^0 corresponds to the mean observed σ^0 value. On the other hand, the slice measurements are well suited for simultaneously estimating the incidence and azimuth angle dependence and so can employ the MI24 model and correction strategy. To ensure consistency with the SAR and footprint cases, rather than reporting the estimated model A_0 value, the other model coefficients are used to compute a correction factor that is applied to the individual σ^0 measurements prior to image formation. The reported σ^0 corresponds to the mean of the corrected σ^0 values.

To correct for the azimuth and incidence angle of a particular measurement, the weighted forward projection of each measurement is first computed from the estimated MI24 model parameter images using the measurement's MRF. In this computation, the A_0 term is not included. The estimated σ^0 variation due to the azimuth and incidence angle is subtracted from the σ^0 measurement, yielding a "corrected" measurement. The corrected measurement is then used for computing the GRD or SIR images of the mean σ^0 . This approach provides the higher resolution σ^0 images than merely using the original MI24 A_0 model value.

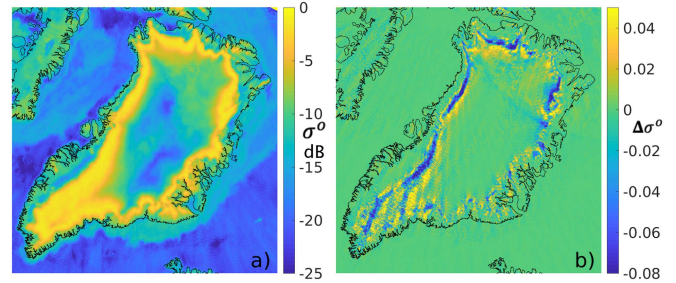


Fig. 14. (a) Eight-day evening, HH pol slice SIR σ^0 in dB. On this scale, the azimuth corrected and nonazimuth corrected appear similar. (b) Linear difference between the model-corrected σ^0 and uncorrected SIR images.

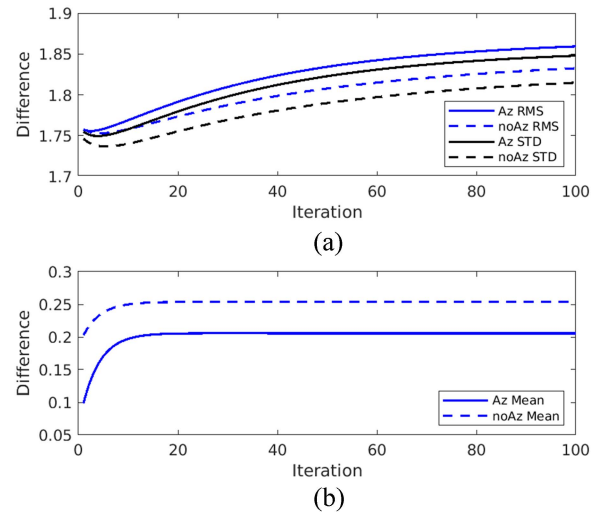


Fig. 15. Plot of difference between slice SIR σ^0 and SAR GRD σ^0 values for Greenland evening HH images using M and MI24 models. (a) Difference RMS and STD. (b) Mean difference. Computed in linear space.

The resulting corrected σ^0 image has fewer artifacts than an uncorrected image. Fig. 14 shows an SIR image computed from corrected slice σ^0 measurements and a difference image between corrected and uncorrected images. Note that the chief differences occur in the melt zones along the edges of the Greenland ICE SHEET, an area of great geophysical interest. Together, the model-corrected image and the model parameters images more accurately describe the scattering characteristics of the surface in these areas.

E. Selection of the Number of SIR Iterations

Fig. 15 shows the difference between the SAR reference image and the SIR image versus the number of SIR iterations. Example images from the iteration are shown in Fig. 16. Note the initial decline in the root mean square (RMS) and standard deviation (std), followed by a slow rise. This is because each SIR iteration not only improves the signal error, but also enhances the noise. During the initial drop, the improvement in the signal component of the difference is larger than the rising noise level. As iteration continues, the noise component begins to dominate. While the minimum error occurs at four or five iterations,

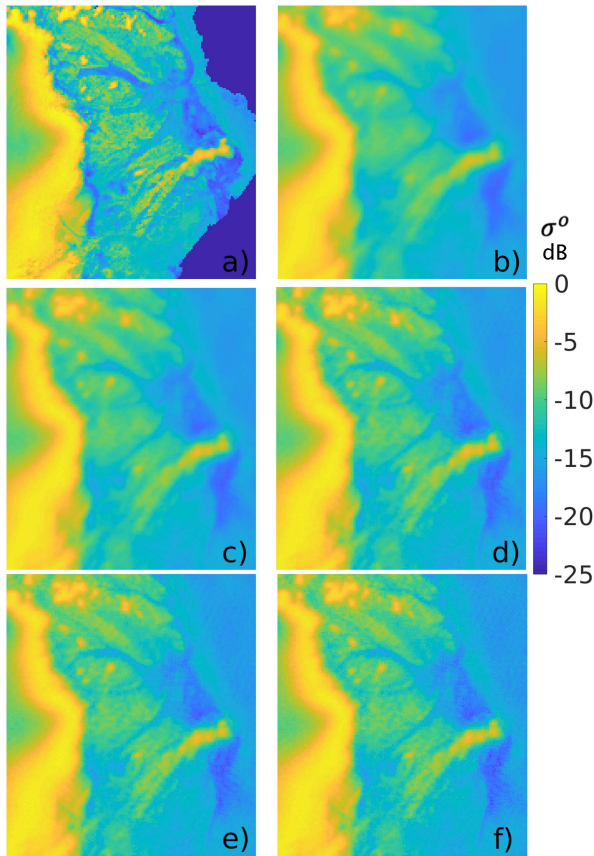


Fig. 16. Zoom-in σ^0 comparison images in dB. (a) SAR GRD. (b) AVE (first SIR iteration). (c) Five SIR iterations. (d) 20 SIR iterations. (e) 50 SIR iterations. (f) 100 SIR iterations. Location of this study area is indicated in Fig. 1.

subjectively, the image continues to improve for a while. Noting that the mean difference stabilizes by about 20 iterations, this value is selected for processing the full dataset.

V. EFFECTIVE RESOLUTION

Image comparisons shown in Figs. 6, 7, and 16 confirm that SAR measurements provide the finest spatial resolution, while the footprint measurements have the coarsest resolution. They also reveal that SIR reconstruction improves the effective resolution of the slice and footprint measurements. To quantify the effective resolution of the various images, a vertical section line over a narrow bright ridge in Northeast Greenland is considered (see Fig. 6 for location). This provides an impulse-like image from which the 3-dB width of the PSRF can be estimated. Fig. 17 plots the σ^0 values from the SAR, slice, and footprint images. The SAR image has a higher narrower peak than the other images. To estimate the effective resolution, the 3-dB width of the peak is determined for each case and normalized by the SAR image 3-dB width. The resulting estimated effective resolutions are approximately 5 km for the slice SIR, 6 km for the slice AVE, and 9 km for the footprint SIR. The SAR GRD resolution is 3.125 km. To further understand the effective resolution of the enhanced resolution slice SIR images, a point-like bright σ^0 target with a high contrast with the surrounding terrain is

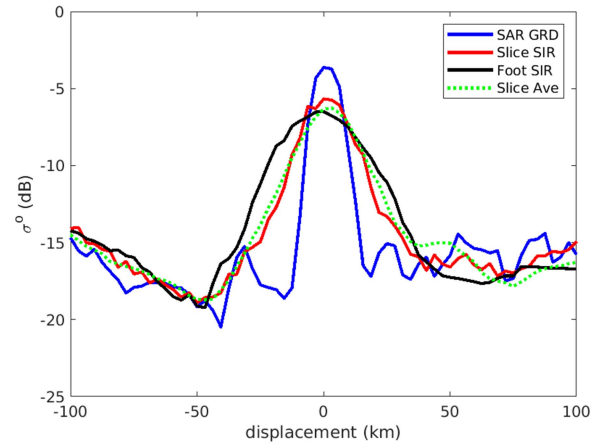


Fig. 17. Plots of σ^0 along the vertical section line indicated in Fig. 6 for the various images. The SAR image has been slightly vertically shifted to better align the peaks.

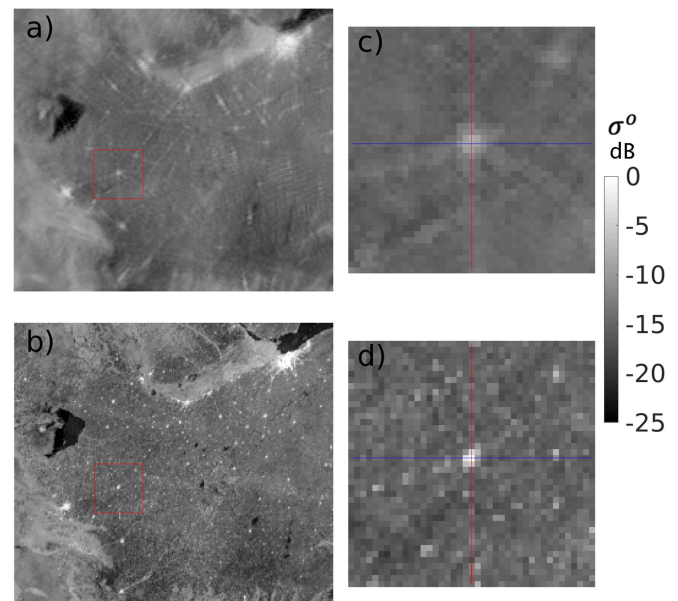


Fig. 18. Sequence of zoom-in σ^0 comparisons of eight-day 3.125-km slice and SAR images for the Argentine study area. For the general location of study area, see Fig. 1. (a) Slice SIR. (b) SAR GRD. (c) Zoom-in of slice SIR. (d) Zoom-in of SAR GRD. Colored lines indicate where sections of the pixels are extracted and plotted in Fig. 19.

identified. A particularly interesting example is the city of Villa Maria, Argentina, which is located east of Buenos Aires. Like other cities in the area, the city exhibits a high σ^0 value, while the surrounding plain has a much lower σ^0 value; see the SAR images in Fig. 18. Cities and roads interconnecting them are apparent in the SAR image. The city of Villa Maria is a few 3.125-km SAR pixels in size. By comparison, the city appears broader and with a lower peak in the slice SIR image.

Fig. 19 shows vertical and horizontal section lines of the slice and SAR images. To aid in the analysis, two smoothed SAR image sections are also included. The smoothed values are computed using 3 pixel and 5 pixel moving average filters.

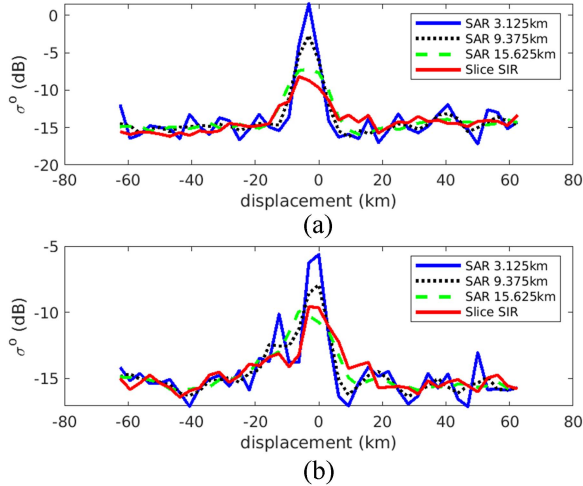


Fig. 19. Plots of σ^0 along the vertical and horizontal section lines indicated in Fig. 18 for (a) vertical and (b) horizontal sections.

The smoothed values correspond to low-pass filtering the 3.125-km/pixel SAR image down to 9.375- and 15.625-km resolution, respectively. Note that while the peak of the slice section is lower than in the SAR image, the 3-dB width of the slice peak corresponds to the 3-dB width of the 9.375-km SAR section. Furthermore, though the slice and 15.624-km SAR sections have similar peak heights, the 3-dB width of 15.625-km SAR peak is wider than the slice peak. This behavioral difference is attributed to the partial reconstruction used in the SIR processing. Based on the 3-dB width, for this case, the effective resolution of the eight-day slice SIR image is approximately 10 km. The difference between this value and the previous estimate is that this target is more point-like compared to the ridge in the previous case. Similar behavior is seen in the other image types, with an estimated footprint SIR resolution of approximately 20 km.

VI. CONCLUSION

This article described the use of SMAP radar data to create a new and unique twice-daily set of image products designed for use in climate studies, particularly in the polar regions. The product employs both conventional DIB gridding techniques and image reconstruction techniques to create both conventional and enhanced resolution backscatter images. The highest resolution σ^0 images are created from SAR measurements with an effective image resolution of 3.125 km, but these images have coverage gaps, including no coverage of Antarctica. Slice and footprint images provide global coverage on the same grids, albeit at lower resolution. By employing resolution enhancement algorithms, the effective resolution of the slice and footprint images is improved to 5–10 and 9–20 km, respectively. In addition, a simple model for the variation of σ^0 with incidence and azimuth angle is used with slice measurements to provide global images of the backscatter model parameters. These parameters can provide insight into surface geophysical processes such as wind-generated snow dunes. The data products

TABLE IV
AVAILABLE TWICE-DAILY SMAP IMAGE PRODUCTS

Type	days	Algorithm	Resolution	Regions*	Corrections
SAR	1	GRD	3.125 km	NST	
SAR	8	GRD	25 km	NST	
SAR	8	GRD	3.125 km	NST	
Slice	1	GRD	25 km	NST	
Slice	3	GRD	25 km	NST	
Slice	8	GRD	25 km	NS	Y
Slice	1	AVE	3.125 km	NST	
Slice	3	AVE	3.125 km	NST	
Slice	8	SIR	3.125 km	NS	Y
Footprint	1	GRD	25 km	NST	
Footprint	3	SIR	25 km	NST	

produced by this research are freely available from the NSIDC (<https://nsidc.org/data/NSIDC-0738/versions/1>) [9].

APPENDIX A

AVAILABLE CETB SMAP RADAR PRODUCTS

SMAP radar data extend from day 103 to day 186 in 2015. During the initial eight days, default SAR data selection tables were used. These provided small even-spaced patches of SAR data. Later, the control tables were updated to collect data over most land regions. Images were made with all available radar data not flagged as “bad.” No calibration corrections were applied to the data. Table IV summarizes available CETB SMAP radar products, which are all in CETB-standard *EASE-2 Grid* projections. Data products from this research are available from NSIDC (<https://nsidc.org/data/NSIDC-0738/versions/1>) [9].

APPENDIX B

AVE AND SIR ALGORITHM DESCRIPTIONS

The goal in forming a σ^0 image map is to estimate the backscatter properties of the surface from noisy measurements that employ (possibly variable) MRFs that sample the surface. Though simple to implement, DIB techniques ignore the MRF. Reconstruction techniques that use the MRF can provide much finer effective resolution.

Reconstruction processing techniques effectively assume that the underlying signal (the backscatter) being sampled is band-limited, which is the only consistent assumption possible with sampled data. For reconstruction, the backscatter at each point of a fine-scale pixel grid is estimated, producing a backscatter image or map. While the image is generated on a regular grid, the measurement locations are not aligned with the grid, and therefore, the measurements form an irregular sampling pattern, which can complicate signal reconstruction.

An individual scatterometer backscatter measurement z_i can be modeled as the integral of the product of the MRF and the surface backscatter, i.e.,

$$z_i = \iint \text{MRF}_i(x, y; pp) \sigma^0(x, y, \theta, \phi_i, t, pp) dx dy + \text{noise} \quad (2)$$

where $\text{MRF}_i(x, y; pp)$ is the spatial MRF of the i th measurement at x, y and the surface σ^0 depends on spatial location x, y , incidence angle θ , azimuth angle ϕ , time t , and polarization

pp , i.e.,

$$\text{MRF}_i(x, y; pp) = \iint \frac{G_a^2(x, y; pp)G_p(x, y; pp)}{R^4(x, y)} dx dy \quad (3)$$

where

$$X = \iint \frac{G_a^2(x, y; pp)G_p(x, y; pp)}{R^4(x, y)} dx dy \quad (4)$$

where $G_a(x, y; pp)$ is the effective two-way antenna gain at the surface at (x, y) for polarization pp , $G_p(x, y; pp)$ is the processor gain, and $R(x, y)$ is the slant range from the radar to the surface. Note that the measurement is an average of σ^0 in spatial coordinates as well as in azimuth and incidence angles.

Equation (2) is discretized on the imaging grid to become

$$z_i = \sum_{j \in \text{image}} h_{ij} a_j + \text{noise} \quad (5)$$

where a_j is the backscatter at the center of the j th pixel and $h_{ij} = \text{MRF}(x_l, y_k; \phi_i)$ is the discretely sampled MRF for the i th measurement evaluated at the j th pixel center, where h_{ij} is normalized so that $\sum_j h_{ij} = 1$. In practice, the MRF is negligible some distance from the measurement center, so the sums need only to be computed over a small area around the pixel. Ignoring the noise, (5) can be written as the matrix equation

$$\vec{Z} = \mathbf{H}\vec{a} \quad (6)$$

where \mathbf{H} contains the sampled MRF for each measurement and \vec{Z} and \vec{a} are vectors composed of the measurements z_i and a_j , respectively. Even for small images, \mathbf{H} is large and sparse and may be over- or underdetermined depending on the number and locations of the measurements. Reconstruction of the surface σ^0 is equivalent to inverting (6).

The iterative SIR algorithm [20], [25] is a particular reconstruction algorithm that is specifically developed for scatterometer image formation. SIR approximates a maximum-entropy solution to an underdetermined equation and a least-squares solution to an overdetermined system. The first iteration of SIR is termed ‘‘AVE’’ (for weighted AVErage) and provides a simple reconstruction estimate that is refined in later SIR iterations. The AVE estimate of the j th pixel is given by

$$a_j = \frac{\sum_i h_{ij} z_i}{\sum_i h_{ij}} \quad (7)$$

where the sums are over all measurements that have nonnegligible MRF at the pixel.

The SIR iteration begins with an initial image a_j^0 whose pixels are set to the AVE values defined in (7). Thereafter, the iterative equation for single-variate SIR is given by

$$a_j^{k+1} = \frac{\sum_i u_{ij}^k h_{ij}}{\sum_i h_{ij}} \quad (8)$$

where

$$u_{ij}^k = \begin{cases} \left[\frac{1}{2p_i^k} \left(1 - \frac{1}{d_i^k} \right) + \frac{1}{a_j^k d_i^k} \right]^{-1}, & d_i^k \geq 1 \\ \frac{1}{2} p_i^k (1 - d_i^k) + a_j^k d_i^k, & d_i^k < 1 \end{cases} \quad (9)$$

$$d_i^k = \left(\frac{z_i}{p_i^k} \right)^\lambda \quad (10)$$

where $d_i^k = (s_i/p_i^k)^\lambda$ with $\lambda = \frac{1}{2}$. The factor d_i^k is the square root of the ratio of a measurement to its forward projection at the k th iteration. The update term u_{ij}^k is a nonlinear function of both d_i^k and the previous image a_j^k . The sigmoid-like nonlinearity in (9) constrains the amount of change permitted during any one iteration, thereby minimizing the effects of noise [25]. Though not used in this article, a spatial median filter can be applied to the image between iterations to further reduce the noise [25].

For scatterometers, SIR is implemented in dB [20], [25], i.e., the computation is done on $10 \log_{10}(z_i)$ rather than on the linear-space value z_i as done in the radiometer version of SIR [12], [13]. In considering the differences between linear and dB processing, recall the well-known fact that computing the arithmetic mean of values in dB is equivalent to computing $10 \log_{10}$ of the geometric mean of the linear-space values [31]. With the measurements in dB, the reconstruction processing can be viewed as a form of weighted geometric mean filtering. Since it has been found that geometric mean filters are better at reducing Gaussian-type noise and preserving linear features than (linear) arithmetic mean filters [32], some performance advantage to dB processing is expected and observed [22]. The linear and dB computations yield similar, but slightly different results, due to the relatively high signal-to-noise ratio of the measurements and limited signal dynamic range.

In practice, since the σ^0 measurements are quite noisy, attempting full image reconstruction can produce excessive noise enhancement. To reduce noise enhancement and resulting artifacts, regularization can be employed at the expense of resolution [20], [26]. Regularization is a smoothing constraint introduced in an inverse problem to prevent extreme values or overfitting. Regularization results in partial or incomplete reconstruction of the signal [26]. It enables a tradeoff between signal reconstruction accuracy and noise enhancement. SIR includes regularization achieved by prematurely terminating the iteration.

REFERENCES

- [1] D. Entekhabi et al., ‘‘The Soil Moisture Active Passive (SMAP) mission,’’ *Proc. IEEE*, vol. 98, no. 5, pp. 704–716, May 2010, doi: [10.1109/JPROC.2010.2043918](https://doi.org/10.1109/JPROC.2010.2043918).
- [2] T. Meissner, L. Ricciardulli, and F. J. Wentz, ‘‘Capability of the SMAP mission to measure ocean surface winds in storms,’’ *Bull. Amer. Meteorol. Soc.*, vol. 98, no. 8, pp. 1660–1677, 2017, doi: [10.1175/BAMS-D-16-0052.1](https://doi.org/10.1175/BAMS-D-16-0052.1).
- [3] C. Derksen et al., ‘‘Retrieving landscape freeze/thaw state from Soil Moisture Active Passive (SMAP) radar and radiometer measurements,’’ *Remote Sens. Environ.*, vol. 194, pp. 48–62, 2017, doi: [10.1016/j.rse.2017.03.007](https://doi.org/10.1016/j.rse.2017.03.007).
- [4] J. Z. Miller, D. G. Long, C. A. Shuman, R. Culberg, M. Hardman, and M. J. Brodzik, ‘‘Mapping firn saturation over Greenland using NASA’s Soil Moisture Active Passive satellite,’’ *IEEE J. Sel. Topics Appl. Earth Observ. Remote Sens.*, vol. 15, pp. 3714–3729, 2022, doi: [10.1109/JS-TARS.2022.3154968](https://doi.org/10.1109/JS-TARS.2022.3154968).
- [5] J. Z. Miller, R. Culberg, D. G. Long, C. A. Shuman, D. M. Schroeder, and M. J. Brodzik, ‘‘An empirical algorithm to map perennial firn aquifers and ice slabs within the Greenland Ice Sheet using satellite L-band microwave radiometry,’’ *The Cryosphere*, vol. 16, pp. 1–23, 2022, doi: [10.5194/tc-14-2809-2020](https://doi.org/10.5194/tc-14-2809-2020).

- [6] J. R. Piepmeier et al., "SMAP L-band microwave radiometer: Instrument design and first year on Orbit," *IEEE Trans. Geosci. Remote Sens.*, vol. 55, no. 4, pp. 1954–1966, Apr. 2017, doi: [10.1109/TGRS.2016.2631978](https://doi.org/10.1109/TGRS.2016.2631978).
- [7] M. J. Brodzik, D. G. Long, M. A. Hardman, A. Paget, and R. Armstrong, "MEaSURES calibrated enhanced-resolution passive microwave daily EASE-Grid 2.0 brightness temperature ESDR, Version 1," NASA NSIDC DAAC, Boulder, CO, USA, 2016, doi: [10.5067/MEASURES/CRYOSPHERE/NSIDC-0630.001](https://doi.org/10.5067/MEASURES/CRYOSPHERE/NSIDC-0630.001).
- [8] R. West, "Soil Moisture Active Passive (SMAP) L1B_S0, L1C_S0, algorithm theoretical basis document (ATBD)," JPL Document 2014. [Online]. Available: https://smap.jpl.nasa.gov/internal_resources/details/original/280_L1C_S0_RevA_web.pdf
- [9] D. G. Long and J. Z. Miller, "SMAP radar SAR and SIR-enhanced twice-daily EASE-Grid 2.0 radar backscatter," NASA DAAC, Nat. Snow Ice Data Center, Digital media, Boulder, CO, USA, 2022. [Online]. Available: <https://nsidc.org/data/NSIDC-0738/versions/1>
- [10] M. J. Brodzik, D. G. Long, and M. A. Hardman, "SMAP radiometer twice-daily rSIR-Enhanced EASE-Grid 2.0 brightness temperatures, version 1.0," Nat. Snow Ice Data Center, Digital Media, Boulder, CO, USA, 2019, doi: [10.5067/QZ3WJNOUZLFK](https://doi.org/10.5067/QZ3WJNOUZLFK).
- [11] M. J. Brodzik and D. G. Long, "Calibrated passive microwave daily EASE-Grid 2.0 brightness temperature ESDR (CETB): Algorithm theoretical basis Document," Nat. Snow Ice Data Center Pub., Boulder, CO, USA, 2018. [Online]. Available: http://nsidc.org/pmestdr/files/MEaSURES_CETB_ATBD_v1.0.pdf
- [12] D. G. Long and M. J. Brodzik, "Optimum image formation for spaceborne microwave radiometer products," *IEEE Trans. Geosci. Remote Sens.*, vol. 54, no. 5, pp. 2763–2779, May 2016, doi: [10.1109/TGRS.2015.2505677](https://doi.org/10.1109/TGRS.2015.2505677).
- [13] D. G. Long and D. L. Daum, "Spatial resolution enhancement of SSM/I data," *IEEE Trans. Geosci. Remote Sens.*, vol. 36, no. 2, pp. 407–417, Mar. 1998, doi: [10.1109/36.662726](https://doi.org/10.1109/36.662726).
- [14] D. G. Long, M. J. Brodzik, and M. Hardman, "Enhanced resolution SMAP brightness temperature image products," *IEEE Trans. Geosci. Remote Sens.*, vol. 57, no. 7, pp. 4151–4163, Jul. 2019, doi: [10.1109/TGRS.2018.2889427](https://doi.org/10.1109/TGRS.2018.2889427).
- [15] J. Piepmeier, P. Mohammed, G. De Amici, E. Kim, J. Pen, and C. Ruff, "Algorithm theoretical basis document: SMAP calibrated, time-ordered brightness temperatures L1B_TB data product," SMAP Project, Rev. A, Dec. 2014. [Online]. Available: https://smap.jpl.nasa.gov/system/internal_resources/details/original/278_L1B_TB_RevA_web.pdf
- [16] M. J. Brodzik, B. Billingsley, T. Haran, B. Raup, and M. H. Savoie, "EASE-Grid 2.0: Incremental but significant improvements for Earth-Gridded data sets," *ISPRS Int. J. Geo-Inf.*, vol. 1, no. 1, pp. 32–45, 2012.
- [17] M. J. Brodzik, B. Billingsley, T. Haran, B. Raup, and M. H. Savoie, "Correction: M.J. Brodzik et al., EASE-Grid 2.0: Incremental but significant improvements for Earth-gridded data sets, *ISPRS Int. J. Geo-Inf.*, vol. 1, no. 1, pp. 32–45, 2012," *ISPRS Int. J. Geo-Inf.*, vol. 3, no. 3, pp. 1154–1156, 2014.
- [18] R. West et al., "SMAP L1C radar half-orbit time-order high-resolution data on 1 km Swath grid, Version 1," NASA, Nat. Snow Ice Data Center Distrib. Active Arch. Center, Boulder, CO, USA, Mar 15, 2023. [Online]. Available: <https://nsidc.org/data/SPL1CSO/versions/1>
- [19] R. West et al., "SMAP L1B radar half-orbit time-order low-resolution data, Version 1," NASA Nat. Snow Ice Data Center Distributed Active Arch. Center, Boulder, CO, USA, Mar 15, 2023. [Online]. Available: <https://nsidc.org/data/SPL1BSO/versions/1>
- [20] D. S. Early and D. G. Long, "Image reconstruction and enhanced resolution imaging from irregular samples," *IEEE Trans. Geosci. Remote Sens.*, vol. 39, no. 2, pp. 291–302, Feb. 2001, doi: [10.1109/36.905237](https://doi.org/10.1109/36.905237).
- [21] F. Ulaby and D. G. Long, *Microwave Radar and Radiometric Remote Sensing*. Ann Arbor, MI, USA: Univ. Michigan Press, 2014.
- [22] D. G. Long, "Comparison of SeaWinds backscatter imaging algorithms," *IEEE J. Sel. Topics Appl. Earth Observ.*, vol. 10, no. 3, pp. 2214–2231, May 2017, doi: [10.1109/JSTARS.2016.2626966](https://doi.org/10.1109/JSTARS.2016.2626966).
- [23] D. G. Long, "Scatterometer backscatter imaging using Backus–Gilbert inversion," *IEEE Trans. Geosci. Remote Sens.*, vol. 57, no. 6, pp. 3179–3190, Jun. 2019, doi: [10.1109/TGRS.2018.2882136](https://doi.org/10.1109/TGRS.2018.2882136).
- [24] D. G. Long and M. R. Drinkwater, "Azimuth variation in microwave scatterometer and radiometer data over Antarctica," *IEEE Trans. Geosci. Remote Sens.*, vol. 38, no. 4, pp. 1857–1870, Jul. 2000, doi: [10.1109/36.851769](https://doi.org/10.1109/36.851769).
- [25] D. G. Long, P. Hardin, and P. Whiting, "Resolution enhancement of spaceborne scatterometer data," *IEEE Trans. Geosci. Remote Sens.*, vol. 31, no. 3, pp. 700–715, May 1993, doi: [10.1109/36.225536](https://doi.org/10.1109/36.225536).
- [26] D. G. Long and R. O. W. Franz, "Band-limited signal reconstruction from irregular samples with variable apertures," *IEEE Trans. Geosci. Remote Sens.*, vol. 54, no. 4, pp. 2424–2436, Apr. 2016, doi: [10.1109/TGRS.2015.2501366](https://doi.org/10.1109/TGRS.2015.2501366).
- [27] I. S. Ashcraft and D. G. Long, "Relating microwave backscatter azimuth modulation to surface properties of the Greenland ice sheet," *J. Glaciol.*, vol. 52, no. 177, pp. 257–266, 2006.
- [28] R. D. Lindsley and D. G. Long, "ASCAT and QuikSCAT azimuth modulation of backscatter over East Antarctica," *IEEE Geosci. Remote Sens. Lett.*, vol. 13, no. 8, pp. 1134–1138, Aug. 2016, doi: [10.1109/LGRS.2016.2572101](https://doi.org/10.1109/LGRS.2016.2572101).
- [29] A. D. Fraser, N. W. Young, and N. Adams, "Comparison of microwave backscatter anisotropy parameterizations of the Antarctic ice sheet using ASCAT," *IEEE Trans. Geosci. Remote Sens.*, vol. 52, no. 3, pp. 1583–1595, Mar. 2014.
- [30] H. Stephen and D. G. Long, "Microwave backscatter modeling of erg surfaces in the Sahara Desert," *IEEE Trans. Geosci. Remote Sens.*, vol. 43, no. 2, pp. 238–247, Feb. 2005, doi: [10.1109/TGRS.2004.840646](https://doi.org/10.1109/TGRS.2004.840646).
- [31] "Geometric mean," Oct. 2016. [Online]. Accessed: http://en.wikipedia.org/wiki/Geometric_mean
- [32] I. Pitas and A. Venetsanopoulos, "Nonlinear mean filters in image processing," *IEEE Trans. Acoust., Speech, Signal Process.*, vol. ASSP-34, no. 3, pp. 573–584, Jun. 1986, doi: [10.1109/TASSP.1986.1164857](https://doi.org/10.1109/TASSP.1986.1164857).



David G. Long (Fellow, IEEE) received the Ph.D. degree in electrical engineering from the University of Southern California, Los Angeles, CA, USA, in 1989.

From 1983 to 1990, he was with the NASA's Jet Propulsion Laboratory (JPL), Pasadena, CA, where he developed advanced radar remote sensing systems. While at JPL, he was the Project Engineer with the NASA Scatterometer (NSCAT) project that flew from 1996 to 1997. He also managed the SCANSAT project, the precursor to SeaWinds that was flown in 1999 on QuikSCAT, in 2002 on ADEOS-II, and in

2014 on the International Space Station. He is currently a Professor with the Department of Electrical and Computer Engineering, Brigham Young University, Provo, UT, USA, where he teaches upper division and graduate courses in communications, microwave remote sensing, radar, and signal processing. He is the Director of the BYU Center for Remote Sensing. He is the Principal Investigator on several NASA-sponsored research projects in remote sensing. He has more than 400 publications in various areas, including signal processing, radar scatterometry, and synthetic aperture radar. His research interests include microwave remote sensing, radar theory, space-based sensing, estimation theory, signal processing, and mesoscale atmospheric dynamics.

Dr. Long has received the NASA Certificate of Recognition several times. He is an Associate Editor for IEEE GEOSCIENCE AND REMOTE SENSING LETTERS.



Julie Z. Miller received the B.S. degree in applied mathematics in 2010 and the M.S. and Ph.D. degrees in geography with a focus on microwave remote sensing of polar ice sheets in 2012 and 2019, respectively, all from the University of Utah, Salt Lake City, UT, USA.

She then completed a Postdoctoral Fellowship with the Byrd Polar and Climate Research Center, Ohio State University, Columbus, OH, USA. She is currently a Research Scientist with the Earth Science and Observation Center, Cooperative Institute for Research in Environmental Sciences, University of Colorado Boulder, Boulder, CO, USA. She has participated in field and airborne campaigns in both Greenland and Antarctica. Her research interests include developing algorithms to map surface and subsurface meltwater in Greenland and Antarctica using multifrequency microwave radiometer and radar scatterometer imagery.

Dr. Miller is a Member of NASA's Soil Moisture Active Passive Science Team.